Characteristics of slow slip events explained by rate-strengthening faults subject to periodic pore fluid pressure changes

Andrea Perez-Silva[1], Yoshihiro Kaneko[2], Martha Savage[1], Laura Wallace[3,4]and Emily Warren-Smith[3]

[1]School of Geography, Environment and Earth Sciences, Victoria University of Wellington, PO Box 600, Wellington 6140, New Zealand.
[2]Department of Geophysics, Kyoto University, Sakyo-ku, Kyoto 606-8501, Japan.
[3]GNS Science, PO Box 30368, Lower Hutt 5011, New Zealand.
[4]Institute for Geophysics, University of Texas, Austin, Texas, USA.

Key Points:

- Periodic pore fluid pressure perturbations on a rate-strengthening fault induce slow slip events (SSEs)
- Source properties of induced SSEs vary with perturbation characteristics (length scale, amplitude, period)
- Model reproduces source properties of shallow Hikurangi SSEs, and duration and magnitude of SSEs in different subduction zones

Corresponding author: Andrea Perez-Silva, andrea.perez@vuw.ac.nz

Abstract

Geophysical observations indicate that temporal pore fluid pressure changes correlate with slow slip events (SSEs) occurring along the shallow portion of the Hikurangi margin and in different subduction zones. These fluctuations in pore fluid pressure are attributed to fluid migration before and during SSEs, which may modulate SSE occurrence. To examine the effect of pore fluid pressure changes on SSE generation, we develop numerical models in which periodic pore-pressure perturbations are applied to a stably sliding, rate-strengthening fault. By varying the physical characteristics of the pore-pressure perturbations (amplitude, characteristic length and period), we find models that reproduce shallow Hikurangi SSE properties (duration, magnitude, slip, recurrence) and SSE moments and durations from different subduction zones. The stress drops of modeled SSEs range from ∼20-120 kPa while the amplitudes of pore-pressure perturbations is several MPa, broadly consistent with those inferred from observations. Our results indicate that large permeability values of $\sim 10^{-14}$ to 10^{-10} m^2 are needed to reproduce the observed SSE properties. Such high values could be due to transient and localized increases in fault zone permeability in the shear zone where SSEs occur. Our results suggest that SSEs may arise on faults in rate-strengthening frictional conditions subject to pore-pressure perturbations.

Plain Language Summary

Slow slip events (SSEs), with slower velocities and longer durations than regular earthquakes, have been detected at several subduction zones worldwide. Recent observations have led researchers to infer that pore fluid pressure —the pressure of fluids in the pore space of rocks—changes during SSEs that occur along the shallow (<15 km depth) portion of the Hikurangi subduction zone, where the Pacific Plate subducts beneath the Australian plate. Similar observations have been reported during SSEs in different subduction zones. However, how pore fluid pressure changes are linked to SSEs is poorly understood. To investigate this issue, we develop physics-based models in which periodic changes in pore fluid pressure are imposed on a fault governed by the expected frictional behavior of rocks derived from laboratory experiments. These pore fluid pressure changes induce SSEs, and the features of these events (duration, magnitude, peak velocity, recurrence interval) change with the characteristics of the pore fluid pressure change (size, amplitude, and period). After exploring different perturbation characteristics, we find models that capture the observed features of SSEs along the Hikurangi margin and in different subduction zones. This study suggests that pore fluid pressure changes may play an important role in SSE occurrence.

1 Introduction

Indirect geophysical observations have suggested that temporal variations in pore fluid pressure correlate with the occurrence of slow slip events (SSEs) in subduction zones such as Hikurangi (Warren-Smith et al., 2019), Cascadia (Gosselin et al., 2020), Nankai (Kita et al., 2021) and Sagami (Nakajima & Uchida, 2018). Such observations indicate that pore-pressure changes are cyclical, coinciding with SSE recurrence time, which suggests that they may play an important role in SSE occurrence. Pore-pressure cycling has been well characterized during SSEs occurring along the shallow (<15 km) portion of the northern Hikurangi margin (offshore Gisborne), where the Pacific plate subducts beneath the Australian plate. Taking measurements of earthquake focal mechanisms within the subducting Pacific slab during four of these SSEs, Warren-Smith et al. (2019) uncovered temporal changes in the relative magnitude of the principal stresses. These changes, used as a proxy for pore pressure, revealed a cycle that coincided with the timing of shallow Hikurangi SSEs. During this cycle, pore pressure increases before SSEs and drops at the onset of SSE slip (bottom inset in Figure 1a).

Pore-pressure cycling during SSEs has been explained through the fault valve model (Gosselin et al., 2020; Warren-Smith et al., 2019). In this model, episodes of fluid accumulation and drainage are driven by the feedback between fault slip, and healing and sealing processes, which modulate permeability changes along the plate interface (Sibson, 1990, 1992). Fluids, derived from dehydration reactions of the subducting plate (e.g., Hyndman & Peacock, 2003; van Keken et al., 2011), accumulate within the slab, trapped by the low permeability seal at the plate interface (Audet et al., 2009; Peacock et al., 2011). Continued fluid accumulation builds up overpressure, which in reaching near-lithostatic values breaks the low-permeability seal, inducing slip at the plate interface. The onset of slip opens fractures that act as pathways for fluid migration, which causes a drop in pore fluid pressure (Figure 1a). The cycle continues as mineral precipitation within newly-opened fractures re-establishes the low-permeability barrier. Tentative evidence of this process is documented in exhumed subduction zones, where so-called crack-seal veins signal episodes of fracturing and sealing (e.g., Behr & Bürgmann, 2021; Condit & French, 2022). Likewise, variations in seismic anisotropy has been attributed to fluid migration through such fractures (Zal et al., 2020; Wang et al., 2022). Notably, the inferred pore-pressure change in these cycles is of several MPa (Gosselin et al., 2020; Warren-Smith et al., 2019), while the stress drop of most SSEs ranges from 0.01 to 0.1 MPa (Gao et al., 2012). Such discrepancy is not intuitive and calls for an explanation.

Within the standard rate-and-state friction (RSF) framework (Dieterich, 1979), SSEs commonly require rate-weakening friction to nucleate, while different mechanisms (e.g., transition to rate-strengthening friction, Shibazaki, 2003; dilatancy strengthening, Segall et al. 2010; transitional friction behavior, Liu and Rice, 2007) have been proposed to stabilize the growing unstable slip. These models, although successful in reproducing SSE characteristics (e.g., Liu & Rice, 2009; Li & Liu, 2016; Matsuzawa et al., 2013; Perez-Silva et al., 2021, 2022; Shibazaki et al., 2012, 2019; Dal Zilio et al., 2020), do not account for the temporal variation in pore pressure nor the widespread occurrence of rate-strengthening materials in slow slip regions (e.g., Bürgmann, 2018; Ikari et al., 2013; Saffer & Wallace, 2015). An alternative modeling approach, proposed by Perfettini and Ampuero (2008), suggests that transient slip is induced in rate-strengthening conditions by external stress perturbations. This approach is consistent with recent numerical models in which changes in pore pressure within rate-strengthening fault zones give rise to aseismic slip (e.g., Dublanchet, 2019; Heimisson et al., 2019; Mallick et al., 2021; Yang & Dunham, 2021).

Recent modeling efforts have focused on the relation between fluids and fault slip to explain different phenomena. In a model that coupled fluid flow, permeability and pore-pressure evolution with RSF, Zhu et al. (2020) found that fluid pressurization induced earthquake swarms and aseismic slip at different parts of the seismogenic zone. In another model, in which changes in permeability through fault valving modulated pore-pressure diffusion, Farge et al. (2021) captured realistic tremor-like patterns. Using a different approach, Bernaudin and Gueydan (2018) explained episodic tremor and slip (ETS) characteristics by modeling a brittle-ductile material, governed by microfracturing, sealing and fluid pumping. Yet other models propose that traveling porosity waves carrying elevated pore-pressure (Skarbek & Rempel, 2016), and pore pressure waves (Cruz-Atienza et al., 2018) may control the periodicity of ETS, and the speed of rapid tremor migrations, respectively. All these studies have focused on describing the mechanism whereby pore pressure and fault slip are coupled. However, since they assume either 1-D or 2-D models, direct comparison to observations has been limited.

In this work, we explore the possibility that periodic pore-pressure perturbations in a rate-strengthening fault zone induce SSEs with source properties (duration, magnitude, peak velocity, recurrence interval, slip) comparable to observations. We assume a relatively simple modeling approach in which fault slip relates to pore-pressure changes through changes in effective stress —the difference between the lithostatic load and pore

fluid pressure. Our model targets shallow SSEs in the northern part of the Hikurangi margin (offshore Gisborne), as pore-pressure fluctuations during these events are well-characterized (Wang et al., 2022; Warren-Smith et al., 2019; Zal et al., 2020). In addition, we investigate whether SSEs in other subduction zones can be explained using the same modeling approach.

2 Model Setup

2.1 Fault model

Our modeling approach is built upon the one developed by Lapusta and Liu (2009). Our model consists of a planar fault embedded in an elastic medium and loaded by a long-term plate rate at the upper and lower ends of the fault along depth (z). Fault slip is governed by the balance between the frictional strength and the shear stress on the fault (Text S1). The frictional strength, τ, is given by the following equation:

$$\tau(x, z; t) = f[\sigma - \Delta p_{\mathrm{f}}(x, z; t)] \tag{1}$$

where f is the friction coefficient, σ is the background normal stress and Δp_{f} is the pore fluid pressure change. Pore-pressure perturbations are imposed by varying the effective normal stress ($\sigma - \Delta p_{\mathrm{f}}$), where σ is constant and Δp_{f} evolves in time and space (Section 2.3). We assume pore-pressure changes and fault slip are related via changes in effective normal stress (i.e., one-way coupling).

The evolution of the friction coefficient f is governed by the laboratory-derived rate-and-state friction laws (Dieterich, 1979; Ruina, 1983), that describe f as a logarithmic function of the slip rate V and a state variable θ:

$$f = f_0 + a \ln(V/V_0) + b \ln(V_0\theta/L) \tag{2}$$

where f_0 is the steady state friction coefficient at reference rate V_0, d_c is the characteristic slip for state evolution, V is the slip rate, and a and b are the direct and evolution effect, respectively. The evolution of the state variable is assumed to follow the aging law (Marone, 1998; Dieterich, 1979):

$$\frac{d\theta}{dt} = 1 - \frac{V\theta}{d_c}. \tag{3}$$

2.2 Fault model parameters

Model parameters are given in Table 1. The fault is loaded by a uniform plate rate (V_{pl}) of 50 mm/yr, consistent with the estimated convergence rate offshore Gisborne, in the northern Hikurangi margin (Wallace et al., 2004). To account for the shallow depths of SSEs, we set the shear modulus (μ) to 10 GPa, which is within the range (6–14 GPa) inferred at the central Hikurangi margin using full-waveform inversion of controlled-source seismic data (Arnulf et al., 2021). The Poisson's ratio is set to 0.25, corresponding to a Poisson solid.

We consider uniform friction properties on the fault, where $a = 0.005$ and $b = 0.004$ ($a/b = 1.25$); these values are within the range (10^{-4} to 10^{-2}) obtained in friction experiments on incoming sediments to the Hikurangi margin (e.g., Boulton et al., 2019; Eijsink & Ikari, 2022; Ikari et al., 2020). These experiments show that frictional stability trends span rate-strengthening, rate-neutral, and rate-weakening behaviors. In this study, we focus exclusively on rate-strengthening friction. Unstable slip under rate-strengthening conditions can initiate due to external stress perturbations (Perfettini & Ampuero, 2008). In our model, the increase in pore pressure reduces fault strength, thus promoting slip.

The spatial discretization must resolve the characteristic size of the process zone $L_b = \mu d_c / b\sigma$ (Ampuero & Rubin, 2008; Perfettini & Ampuero, 2008), equivalent to 4.17 km

for all simulations presented. The grid spacing Δx is chosen as a fraction of L_b, typically $\Delta x = L_b/5$. Each simulation takes from 20 minutes up to 4 hrs on 64 physical cores of the New Zealand eScience Infrastructure's Cray XC50 computer. To save computational costs we set the background normal stress (σ) to 3 MPa, which is below the estimated range (10-30 MPa) along the shallow Hikurangi margin (Arnulf et al., 2021). We could scale up σ by reducing the constitutive parameters a and b so that $a\sigma$ and $b\sigma$ remain constant, and obtain the same results, as expected from Equations 1 and 2 (e.g., Perez-Silva et al., 2022).

2.3 Models of pore-pressure cycling

To model the inferred pore-pressure cycling, we impose periodic perturbations in pore pressure on a rate-strengthening planar fault, as schematically shown in Figure 1b. We define two types of perturbations to describe the evolution of pore pressure in space and time, as explained in the following. Note that the recurrence interval of shallow Gisborne SSEs is determined by the period of the pore-pressure cycle, as proposed by Warren-Smith et al. (2019). As shallow Gisborne SSEs recur every ∼2 yrs (Wallace & Beavan, 2010; Wallace, 2020), we set the perturbation period T_{per} to 2 yrs.

2.3.1 Type I perturbation: Sawtooth-like pore-pressure changes

Within the subducting slab, temporal pore-pressure changes were proposed to follow a 'sawtooth' pattern during shallow Hikurangi SSEs (bottom inset in Figure 1a, Warren-Smith et al., 2019). Following this study, we define the temporal evolution of pore pressure as shown in Figure 1c. For simplicity, the spatial pore-pressure change is defined as a gaussian distribution (Figure 1e). Even though we do not model fluid flow in this case, we envision that it is normal to the fault.

The evolution of pore pressure in space and time is given by:

$$\Delta p_{\text{f}}(r, t^*) = \Delta p_{\max} \exp\left(\frac{r^2}{r^2 - R_0^2}\right) \left[\frac{t^*}{T} H(T - t^*) + e^{-C(t^* - T)} H(t^* - T)\right] \quad \text{for } r < R_0, \tag{4}$$

where Δp_{f} is the pore-pressure change in MPa, r is the radial distance from the fault center in km, t^* is the time since the start of the perturbation in yrs, $\Delta p_{\max}$ is the maximum pore-pressure change in MPa, R_0 is the perturbation radius in km and T its duration in yrs. C represents the exponential decay rate of pore pressure, which we set to 10 yr^{-1} to model the inferred rapid decrease in Δp_{f} (bottom inset in Figure 1a). $H(t)$ is the Heaviside function; $H(t) = 0$ for $t < 0$ or $H(t) = 1$ for $t > 0$. Equation (4) shows that the size and amplitude of perturbations are controlled by R_0 and $\Delta p_{\max}$. Following Perfettini and Ampuero (2008), we express them in terms of non-dimensional parameters R_0/L_b and $\Delta p_{\max}/a\sigma$, respectively.

2.3.2 Type II perturbation: Along-fault fluid diffusion

The second type of perturbation is motivated by fluid injection experiments (Guglielmi et al., 2015; Cappa et al., 2019) and numerical models (Dublanchet, 2019; Larochelle et al., 2021; Yang & Dunham, 2021; Zhu et al., 2020), in which aseismic slip is induced by the injection of fluids that diffuse into the fault zone. In this perturbation, fluid flow is driven by diffusion along the fault plane, while there is no flow in the fault-normal direction. We prescribe that fluids are injected into the fault plane from the wall of a circular cylinder of radius r_0, perpendicular to the fault plane. Fluid flow occurs only within the fault plane and is fault-parallel and axis-symmetry with respect to the axis of the circular cylinder (Sáez et al., 2022). Fluid is injected at a constant rate q_0 (in m/s) and

diffuses along the fault plane following the axis-symmetric fluid diffusion equation:

$$\frac{\partial p_{\mathrm{f}}(r,t)}{\partial t} = D\left(\frac{\partial^2 p_{\mathrm{f}}(r,t)}{\partial r^2} + \frac{1}{r}\frac{\partial p_{\mathrm{f}}(r,t)}{\partial r}\right) \tag{5}$$

where r is the radial distance in km and D is the hydraulic diffusivity in m^2/s, which we assume is uniform on the fault plane. For simplicity, our model does not account for permeability and porosity evolution, which may also affect the fault response (Zhu et al., 2020; Yang & Dunham, 2021). In the time domain, the solution of Equation 5 can be expressed in the following functional form:

$$p_{\mathrm{f}}(r,t) = \frac{q_0 r_0}{D\phi\beta}\,\Pi(r,t) \tag{6}$$

where ϕ is the porosity and β is the sum of the pore and fluid compressibility. Π is the dimensionless pore-pressure evolution given by (section 13.5, eq. 17, Carslaw & Jaeger, 1959):

$$\Pi(r,t) = -\frac{2}{\pi}\int_0^\infty \left(1 - e^{-Du^2 t}\right)\frac{J_0(ur)Y_1(ur_0) - Y_0(ur)J_1(ur_0)}{u^2[J_1^2(ur_0) + Y_1^2(ur_0]}du \tag{7}$$

where J_i and Y_i are respectively the Bessel function of the first and second kind of order i, where $i = 0$ or 1. To model the pore-pressure perturbation, we use the exact solution of Equation 7 solved via numerical inversion of the Laplace transform (Stehfest, 1970; Cheng, 2016). We note that Equation 7 is valid for $r \geq r_0$.

The evolution of pore-pressure during the perturbation is given by:

$$\Delta p_{\mathrm{f}}(r,t^*) = \frac{q_0 r_0}{\phi\beta}\left[\frac{1}{D}\Pi(r,t^*)H(t^*) - \frac{1}{D_b}\Pi(r,t^* - t_{\mathrm{inj}})H(t^* - t_{\mathrm{inj}})\right], \tag{8}$$

where t_{inj} is the time over which fluids flow into the fault plane, and D and D_b are the hydraulic diffusivity before t_{inj} and after t_{inj}, respectively. Equation 8 shows that fluids diffuse from the cylinder wall along the fault plane over time t_{inj}, thus increasing pore pressure. After t_{inj}, pore-pressure decreases as fluids diffuse away from the fault with diffusivity D_b, where $D_b > D$ (Figures 1d and 1f). This perturbation is characterized by t_{inj}, D, D_b, r_0 and $q_0/\phi\beta$, where the latter is treated as a free parameter.

Similar to type I case, the perturbation characteristics are its size and amplitude. The size of the perturbation is controlled by the diffusion length $\sqrt{Dt_{\mathrm{inj}}}$, which represents the evolution of the pore-pressure front, while the maximum pore-pressure change $\Delta p_{\max}$ determines its amplitude. We define D, t_{inj} and $\Delta p_{\max}$ as input parameters. To obtain a given $\Delta p_{\max}$, we solve for $q_0/\phi\beta$ using Equation 8. The normalized perturbation size and amplitude correspond to $\sqrt{Dt_{\mathrm{inj}}}/L_b$ and $\Delta p_{\max}/a\sigma$, respectively. We note that the characteristic length scale of the diffusion process is $\sqrt{Dt_{\mathrm{inj}}}/r_0$. However, to account for the effect of the fault properties, we consider L_b instead of r_0 in the characteristic length of the perturbation ($\sqrt{Dt_{\mathrm{inj}}}/L_b$), consistent with type I case (R_0/L_b). The length scale r_0 could be interpreted as the width of the fluid source. Unless otherwise noted, we assume $r_0 = 1$ km to ensure that r_0 is properly resolved by our simulations ($\Delta x_{\max} = 0.78$ km, Table 1). In Section 5.1, we comment on the implications of different r_0. Note that, since Equation 7 is valid for $r \geq r_0$, we simply assume a constant value $\Delta p_{\mathrm{f}}(r_0, t^*)$ within $0 < r < r_0$.

3 Fault response to periodic pore-pressure perturbations

We find that periodic pore-pressure perturbations of type I and II can induce SSEs, whose recurrence interval is controlled by the period of the perturbation. We explore the controlling parameters of each perturbation type (size: R_0/L_b or $\sqrt{Dt_{\mathrm{inj}}}/L_b$, and amplitude: $\Delta p_{\max}/a\sigma$) and its effects on induced SSE properties in Section 4 (Table S1).

Based on the parameter exploration, we find two representative models (one for each perturbation type) that induce SSEs with properties comparable to the those of shallow Gisborne SSEs, which are duration of 6-34 days, M_w6.2-6.5, maximum slip of 4-27 cm and recurrence of ∼2 yrs (Ikari et al., 2020). The perturbation characteristics for each representative model are given in Table 2, while Table 3 compares modeled and observed Gisborne SSE properties. Note that the representative models are non-unique, as different parameter combinations lead to SSEs with source properties comparable to the observed range. In the following, we describe the fault response for these two models.

3.1 Representative model for type I perturbation

We impose a pore-pressure perturbation every 2 yrs (red lines in Figure 2a) with $R_0 = 33.8$ km and $\Delta p_{\max} = 1.88$ MPa (Table 2). This perturbation induces SSEs characterized by the transient increase in the maximum slip velocity on the fault ($V_{\max}$, blue lines in Figure 2a).

To visualize the fault response during an induced SSE, we show snapshots of the slip velocity in Figures 2b to 2g (see also Movie S1 and Figure S1) and contours of the pore-pressure change ($\Delta p_f/\sigma$, solid lines). The slip rate evolution can be divided into four consecutive phases: (1) During the last stages of pore-pressure increase ($t^* > 1$ yr), the slip rate accelerates from the edges of the perturbation and propagates towards the center of the fault (Figure 2b to 2c). Meanwhile, the central fault patch, which starts off fully locked (Figure 2b), gradually unlocks as it shrinks down (Figure 2c). In this phase, the friction coefficient increases through rising slip rates to compensate for the decrease in effective normal stress (Equation 1). (2) Slip fronts coalesce at the fault center, rising the slip rate to its peak value (Figure 2d). (3) Slip rate decelerates as slip fronts migrate away from the center (Figure 2e). (4) At the onset of depressurization, the slip velocity rapidly drops within the pressurized area (Figure 2f). In this case, the drop in slip rate balances the increasing effective normal stress; a response opposite to that in phase (1). At the end of the perturbation, the pressurized area is fully locked (Figure 2g). Likewise, in the inter-SSE period the slip rate within the perturbed area is well below V_{pl} ($V/V_{\text{pl}} \sim 10^{-30}$, Figure S1). While these velocities are below the range of slip rates applicable to RSF, there are no observational constraints to distinguish velocities below $\sim 10^{-11}$ m/s.

Interestingly, while the maximum pore-pressure change is of the order of MPa, the maximum stress change during an induced SSE is ∼60 kPa (Figure 2h). This occurs because the shear stress within the pressurized area decreases to a value close to the initial frictional strength, $f_0(\sigma - \Delta p_f(r, t^*))$, after the first perturbation and does not return to its original value in the inter-SSE period due to the relatively short perturbation interval (Figure 2i). In other words, periodic pore-pressure changes cause a redistribution of the shear stress, which then decreases within the pressurized region to compensate for its lower effective stress (or equivalently lower strength).

3.2 Representative model for type II perturbation

We apply a pore-pressure perturbation every 2 yrs (red lines in Figure 3a) with $\sqrt{Dt_{\text{inj}}}$ ~ 8 km and $\Delta p_{\max} = 1.5$ MPa (Table 2). Similar to the previous model, $V_{\max}$ transiently increases in response to the perturbation, signaling SSEs (blue lines in Figure 3a). In contrast to the previous case, SSEs arise shortly after the start of the perturbation. This difference could be attributed to the fact that pore pressure increases over a much shorter time ($t_{\text{inj}} = 30$ days) than for type I model ($T = 1.5$ yrs).

The slip rate evolution on the fault during an induced SSE is illustrated in Figures 3b to 3g, where pore-pressure contours ($\Delta p_f/\sigma$, solid lines) are also drawn (see also Movie S2 and Figure S2). We can again divide the fault response into four consecutive phases.

(1) Slip acceleration localizes at the center of the fault, where the slip rate is maximum (Figure 3b). In this phase, the slip rate increases to balance the decrease in effective stress. (2) Slip acceleration transitions into crack expansion (Figures 3c to 3d), while the maximum slip rate localizes at the crack tip. During this phase, the slow slip front migrates faster than the pore-pressure front; as seen in previous models of fluid-driven aseismic slip (Bhattacharya et al., 2017; Dublanchet, 2019). (3) As pore-pressure decreases, starting from the injection point, two competing effects take place. Around the injection point slip rate decelerates below V_{pl}, whereas away from the injection point crack expansion continues (Figures 3e to 3f). (4) Ongoing depressurization causes deceleration to gain control over the fault response. The slip rate decreases across the fault while the central fault patch remains locked (Figures 3g). Just as for type I case, during depressurization, the slip rate decreases to balance the increasing effective stress (Equation 1). In the inter-SSE period, the fault is fully locked within the perturbed region ($V \ll V_{\mathrm{pl}}$, Figure S2).

Similar to the previous model, shear stress decreases within the perturbed region to a value close to the frictional strength in response to periodic pore-pressure changes and does not recover in the period between perturbations (Figure 3i). The maximum stress change during an induced SSEs is again much lower (∼35 kPa, Figure 3h) than the maximum applied pore-pressure change (1.5 MPa, Table 2).

4 Reproducing shallow Gisborne SSEs

To find the parameter space that reproduced Gisborne SSE properties, we explore the perturbation amplitude and characteristic length, keeping the perturbation period constant ($T_{\mathrm{per}} = 2$ yrs). A limited range of parameters are considered (Table S1), as the exploration targets only Gisborne SSE properties, where pore-pressure cycling has been inferred (Warren-Smith et al., 2019). For each simulation case, we calculate the average source properties of induced SSEs (i.e., duration, magnitude, maximum slip and peak velocity) as explained in the following.

4.1 Calculation of SSE properties

To calculate SSE properties, we first define a velocity threshold (V_{thr}). SSE duration corresponds to the time over which the maximum slip rate on the fault exceeds V_{thr}. We calculate the corresponding SSE moment using the SSE area and the slip accumulated over the SSE duration. To calculate the accrued slip, we sum the slip over the cells with slip larger than the minimum slip, defined as 1.1 $\times V_{\mathrm{pl}} \times$ SSE duration. This definition ensures that the accumulated slip exceeds the slip accrued due to a given plate loading rate over the SSE duration, and hence is applicable for different subduction zones (Section 5).

The value of V_{thr} depends on the resolution of the instrumentation used to detect SSEs. In the case of shallow Hikurangi SSEs, as they occur offshore, GPS resolution is lower (∼2 mm/day) than in other margins where SSEs occur beneath GPS networks (e.g., ∼0.25 to 0.5 mm/day, Wech & Bartlow, 2014). To compare our model results with observed SSE properties at Hikurangi (Table 3), we set V_{thr}= 2 mm/day. In the following section, $V_{\mathrm{thr}} = 0.3$ mm/day, which is why SSE properties show longer duration and magnitudes than constrained by observations at Hikurangi. Setting a lower V_{thr} in this case, allows us to estimate the sensitivity of SSE source properties to the perturbation characteristics.

4.2 Exploration of perturbation characteristics

To investigate the effect of the perturbation amplitude on SSE properties, we explore $\Delta p_{\max}$ from 0.375 MPa to 2.25 MPa ($0.125 < \Delta p_{\max}/\sigma < 0.75$) for both pertur-

bation types. The perturbation size is explored within different ranges for each perturbation type (Table S1). For type I case, R_0 ranges from 11.25 km to 45 km, while for type II, 1.6 km $< \sqrt{Dt_{\text{inj}}} <$ 11.4 km. In the latter case, we explore D from 5 to 50 m^2/s and keep t_{inj}= 30 days, which is within the range of shallow Hikurangi SSE duration (∼6-34 days, Ikari et al., 2020).

Figure 4 summarizes the average SSE properties as a function of the perturbation length scale and amplitude for both type I (Figure 4a to 4f) and type II (Figure 4g to 4l) perturbations. SSE properties increase with the perturbation size in both cases (Figure 4a to 4c and Figure 4g to 4i). For a given size of the perturbation, SSE properties also increase with the perturbation amplitude for type II perturbation (Figure 4j to 4l). This is not the case for type I perturbation, where the perturbation amplitude has a relatively minor effect on SSE properties (Figure 4d to 4f). On the other hand, SSE maximum slip is insensitive to changes in the perturbation characteristics and remains constant (∼10 cm) for all simulation cases shown in Figure 4 (Figure S3).

In all simulations presented so far, we keep a constant $a/b = 1.25$ (Table 1). To investigate the sensitivity of SSE properties to changes in this parameter, we explore a/b from 1.1 to 2.5. We find that larger a/b (i.e., more strengthening conditions) negatively correlate with SSE peak velocity, duration and magnitude (Figure S4), as expected. Just as in Figure 4, the maximum slip remains ∼10 cm (Figure S4). This occurs because the maximum slip mainly depends on the perturbation period and the plate rate, which are kept constant in this exploration.

In some simulation cases (not shown in Figure 4), SSE peak velocities alternate between slow and fast values (e.g., Figure S5). We refer to this behavior 'slip-rate doubling'. Since similar observations have not been made on observed SSEs, we describe this phenomenon in the supplementary information (Text S2).

5 Reproducing the source properties of SSEs in several subduction zones

To investigate whether our modeling approach could reproduce broader SSE properties, we explore further the perturbation characteristics (i.e., perturbation size and period; amplitude was explored in Section 4.2). For this purpose, we select type II (along-fault fluid diffusion) perturbation. Model parameters are as given in Table 1, with the difference that $\mu = 30$ GPa and $\sigma = 9$ MPa to account for the fact that most SSEs occur at deep depths (>20 km).

5.1 Exploration of type-II perturbation characteristics

To explore a broad range of perturbation length scales, we vary D and t_{inj} over a few orders of magnitude, respectively 10^{-1} to 10^2 m^2/s and 10 to $10^{2.9}$ days (or 0.027 to 2 yrs), so that $10^{-1.15} < \sqrt{Dt_{\text{inj}}}/L_b < 10^{1.15}$. To isolate the effect of $\sqrt{Dt_{\text{inj}}}/L_b$ on SSE properties, we set a constant $T_{\text{per}} = 5$ yrs, $\Delta p_{\max}/\sigma = 0.5$ and V_{thr}= 0.3 mm/day. The perturbation characteristics for each simulation case are shown in Table S2. To calculate SSE properties, we use the same approach described in Section 4.1. We plot the average moment and duration of induced SSEs in each simulation in Figure 5a. Note that for a given simulation, emerging SSEs have the same properties. Induced SSEs cover a broad range of durations and moments, from short duration (∼40 days) and low magnitudes (∼M$_w$5.5), to long duration (∼1 yr) and large magnitude (∼M$_w$8). The change in SSE properties positively correlates with $\sqrt{Dt_{\text{inj}}}/L_b$ (Figure 5a).

As shown in Section 3, the period of the perturbation defines the recurrence interval of induced SSEs. Since observed SSE periodicity typically ranges from one to several years (Schwartz & Rokosky, 2007), we impose perturbations with periods ranging from 1 to 8 yrs. For simplicity, we keep $t_{\text{inj}} = 0.5$ yrs and vary D over the same range

shown in Figure 5a. We find that for a given $\sqrt{Dt_{\text{inj}}}/L_b$ (i.e., markers with same shape in Figure 5c), SSE duration and moment increase with the perturbation period. This could be explained by the fact that between perturbations, the fault is strongly locked despite the rate-strengthening condition. Thus, setting a longer perturbation period implies higher strain accumulation, which is released during pore-pressure increase, resulting in SSEs with longer duration and larger magnitude. We note that simulation cases with $D = 10$ or 100 m^2/s and $T_{\text{per}} = 1$ or 2 yrs lead to slip-rate doubling (Text S2), and these results are not shown in Figure 5c.

Apart from the perturbation characteristics, the resolution of GPS networks also affects the estimated SSE duration and moment. In Figures 5a and 5c, we calculate SSE properties assuming $V_{\text{thr}} = 0.3$ mm/day, which is a relatively low threshold (Section 4.1). For comparison in Figure 5b, we consider a higher threshold, V_{thr}= 2 mm/day and calculate SSE properties for the same simulation cases as in Figure 5a. As expected, SSEs have shorter durations and lower magnitudes than previously estimated (c.f. Figure 5a and 5b). Note that only three simulation cases with $D = 0.1$ m^2/s are shown in Figure 5b, as for the other two cases SSE peak velocities fall below V_{thr}.

As mentioned in Section 2.3.2, $r_0 = 1$ km in all simulation cases. Varying this parameter has a minor effect on the perturbation characteristics and induced SSE properties, as discussed in Text S3.

5.2 Comparison to observed SSE moment and duration

Using our modeling approach, we simulate the moment and duration of SSEs in different subduction zones as constrained by observations. We target short-term (i.e., short-duration, low magnitude) SSEs from Cascadia (Michel et al., 2019) and shallow Hikurangi (including SSEs along the whole margin, not only offshore Gisborne) subduction zones, and long-term (i.e., long-duration, large magnitude) SSEs from deep Hikurangi (Ikari et al., 2020; Wallace, 2020), Guerrero (Mexico) (Radiguet et al., 2012) and Nankai (Takagi et al., 2019) subduction zones (Figure 6a). While pore-pressure fluctuations have not been associated with deep Hikurangi SSEs nor long-term Nankai SSEs, we include them here to explore the possibility that these SSEs are also induced by perturbations in pore pressure.

To reproduce the observed SSE duration and moment, we tune the perturbation length scale, period and amplitude (Table S3), where the perturbation period corresponds to the approximate recurrence interval of observed SSEs. For each target SSE, we define V_{pl} and V_{thr} as shown in Table 4. We plot the average duration and moment of modeled SSEs in Figure 6b. Modeled SSEs broadly capture the observed SSE durations and moments (colored lines in Figure 6b). This agreement is remarkable, given that these models are relatively simple. However, the model fails to reproduce the shortest-duration ($\leq$10 days) shallow Hikurangi SSEs. A broader parameter exploration may be needed to find models that capture SSEs with such properties. Note that even though we compare our results with individual SSEs, the models are more representative for repeating (i.e., with the same properties) SSEs.

The trends seen in Figure 5a to 5c can also be distinguished in Figure 6b. Guerrero SSEs, which exhibit the largest magnitudes and durations, arise in simulation cases with the largest perturbation size ($\log_{10}\sqrt{Dt_{\text{inj}}}/L_b = 0.78$ - 0.93). In contrast, lower-magnitude ($M_w < 6.8$) SSEs in Nankai, Cascadia and shallow Hikurangi require smaller perturbation sizes ($\log_{10}\sqrt{Dt_{\text{inj}}}/L_b < 0.44$). Interestingly, shallow Hikurangi SSEs, which exhibit the shortest durations, call for larger perturbations ($\log_{10}\sqrt{Dt_{\text{inj}}}/L_b = -0.15$ - 0.44) than Cascadia and Nankai SSEs ($\log_{10}\sqrt{Dt_{\text{inj}}}/L_b = -0.8$ - 0.15). This is consistent with the use of a higher V_{thr} (Table 4), which causes SSE duration and moment to be underestimated. Examining D and t_{inj} separately (Figure S10), we find that t_{inj} largely controls SSE duration. Long-duration SSE emerge in simulations with $t_{\text{inj}} > 6$

months, while $t_{\text{inj}} \leq 30$ days for short-duration SSEs (Figure S10). Similarly, the magnitude of SSEs of comparable durations increases with D (Figure S10).

To further constrain our results, we calculate the area and stress drop of modeled SSEs and compare them to available observations (Figures 6c and 6c; see also Figure S11). Modeled SSE areas partially overlap with those estimated by observations, excluding Cascadia SSEs (Figure 6c). The model does not capture Cascadia SSE areas because they are markedly elongated, while induced SSE areas are nearly circular. To calculate the stress drop of modeled SSEs, we follow the energy-based approach by Noda et al. (2013) (Text S4). Our results show that the stress drop ranges from ∼20 to 120 kPa (Figure 6d). Modeled SSE stress drops capture those constrained by observations of Nankai SSEs (Takagi et al., 2019). However, they only partially overlap those from shallow and deep Hikurangi SSEs (red lines in Figure 6d).

6 Discussion and conclusions

Our results show that periodic pore-pressure perturbations on a rate-strengthening fault zone induce SSEs broadly consistent with observations. The source properties of induced SSEs (duration, magnitude, slip rate, recurrence interval) vary with the perturbation characteristics (length scale, amplitude, and period, Figures 4 to 6). After exploring two types of pore-pressure perturbations that model either a simplified (type I) or along-fault (type II) fluid migration, we find models that induce SSEs with source properties comparable to those of shallow Hikurangi SSEs (Table 3). The fact that both perturbation types capture the characteristics of these events highlights the non-uniqueness of the model results. Using type II perturbation, we captured the observed moment and duration of SSEs in different subduction zones (Figure 6b). These results suggest that pore-pressure cycling may be a viable mechanism to generate SSEs on rate-strengthening faults.

Pore pressure evolution is markedly different between type I and II perturbations. In the former, the temporal pore pressure evolution has the same pattern inferred within the lower plate along the Hikurangi margin (Section 2.3.1), which implies that the lower plate and the interface shear zone are hydrologically coupled. For type II model, on the other hand, the plate interface is hydrologically decoupled from the subducting slab, as pore pressure evolution is markedly different from type I case. Given the non-uniqueness of the model results, we cannot distinguish between these two assumptions. Likewise, it is also unclear whether near-lithostatic pore pressure changes are required to induce SSEs. For both representative models of shallow Gisborne SSEs, sub-lithostatic pore pressure changes, $\Delta p_{\max}/\sigma = 0.625$ (Type I) or 0.5 (Type II), induced SSEs comparable to observations (Table 2). For the hydrologically coupled case (type I), this implies that sub-lithostatic pore pressure changes may induce SSEs. However, this is not the case for the hydrologically decoupled case (type II), as we cannot rule out that near-lithostatic pore pressure changes are required to break the low-permeability seal at the plate interface (Figure 1a), as predicted by the fault valve model (Gosselin et al., 2020; Sibson, 1990, 2013; Warren-Smith et al., 2019). We compare $\Delta p_{\max}/\sigma$ with inferred pore pressure changes during SSEs by scaling σ to reasonable values for shallow Hikurangi SSEs (10-30 MPa; Arnulf et al., 2021), which gives a $\Delta p_{\max}$ of 6.25-18.75 MPa (Type I) or 5-15 MPa (Type II). Both ranges are comparable to or slightly larger than the estimated change in pore pressure during SSEs (∼1-10 MPa; Gosselin et al., 2020). Thus, we cannot distinguish between these two scenarios based on the estimated $\Delta p_{\max}$. Observational constraints on the hydrological coupling between the lower plate and the plate interface are needed to validate these models.

Our model results indicate that hydraulic diffusivity values in the range of 0.1 to 100 m^2/s are required to generate SSEs comparable to observations (Table S3). These values are several orders of magnitude larger than laboratory and in-situ measurements

in the fault zone —the highest in-situ value reported inside a fault zone being 0.024 m^2/s (Xue et al., 2013). These anomalously high values may be explained by transient and localized changes in fault zone properties before and during slow slip, which may be induced by fractures during slip (Miller, 2015), hydrofracturing (Muñoz-Montecinos et al., 2021) or porosity waves (Skarbek & Rempel, 2016). Indirect observations of fluid migration during slow slip have estimated transient increases in fault zone permeability during SSEs in Mexico (10^{-12} m^2, Frank et al., 2015) and Tokai region (10^{-15} m^2, Tanaka et al., 2010). For comparison, we estimated permeability through the relation $k = D\eta\beta\phi$, where the permeability (k) depends on fluid viscosity (η), porosity (ϕ), the sum of pore and fluid compressibility (β) and the hydraulic diffusivity (D); the latter which we take from our model results (Table S3). Assuming average values for these parameters at subduction zones, the estimated permeability ranges from 5×10^{-14} to 5×10^{-11} m^2 (Table S4). In situ measurements of hydraulic properties within the slow slip fault zone will be required to constrain these results.

The stress drop of modeled target SSEs ranges from ∼20 to 120 kPa (Figure 6d), which is broadly consistent with the range estimated in a worldwide compilation of SSE source parameters (10 kPa to 1000 kPa; Gao et al., 2012). These results are intriguing as these values are only a fraction (<0.03) of the maximum applied pore-pressure change (1.5 MPa to 4.5 MPa, Table S3), which is consistent with observations in that inferred pore pressure change (∼1-10 MPa; Gosselin et al., 2020) is larger than typical SSE stress drop. In our model, this occurs because the shear stress redistributes in the fault plane in response to periodic pore-pressure changes (Section 3). Within the pressurized area, shear stress decreases to a value close to the initial frictional strength during pore-pressure build-up. Notably, the shear stress does not return to its initial (i.e., before the onset of perturbations) value in the inter-SSE period (Figure 3i), as the perturbation period is not long enough for the shear stress to recover completely.

The scaling relations of SSEs have elicited considerable debate due to their association with the mechanics of slow slip. Initially, SSE moment-duration scaling was suggested to follow a linear trend ($M \propto T$; Ide et al., 2007), while recent observations indicated a cubic trend to be more suitable ($M \propto T^3$; Michel et al., 2019; Frank & Brodsky, 2019; Tan & Marsan, 2020). Definite moment-duration scaling trends are not distinguishable in our model results (Figures 5a, 5b, and 6b). Only simulation cases with a given D exhibit trends that range from linear to cubic (Figure 5a and 5c). However, this is not the case for modeled target SSEs, where scaling trends are varied (Figure 6b). Thus, our model results are inconclusive regarding the existence of SSE moment-duration scaling. On the other hand, modeled target SSEs follow a distinct moment-area scaling close to $M \propto A^{1.5}$ (Figure 6c), which is the same as for SSEs in Cascadia (Michel et al., 2019) and regular earthquakes (Kanamori & Anderson, 1975).

Several simplicafications were made in our modeling approach. (1) Induced SSEs exhibit a roughly circular slip distribution. Such simplication would be valid for some SSEs (e.g., shallow Hikurangi SSEs, Guerrero (Mexico) SSEs), while it is not appropriate for elongated SSEs observed in other subduction zones (e.g., Cascadia). (2) Our model only accounts for a one-way coupling between pore pressure and fault slip. Although this serves as a first order approximation, previous models have emphasized that porosity and permeability evolution, including permeability enhancement, may significantly affect fluid-induced slip (e.g. Bhattacharya et al., 2017; Cappa et al., 2018; Yang & Dunham, 2021). (3) We do not explain the mechanism whereby pore-pressure cycling occurs. Even though several mechanisms have been proposed to couple fault slip and fluid processes (e.g., Bernaudin & Gueydan, 2018; Farge et al., 2021; Skarbek & Rempel, 2016; Zhu et al., 2020), it is still uncertain which one governs pore-pressure fluctuations during SSEs. (4) Finally, we do not explore the full fault response under RSF; other state evolution laws are not considered, such as the slip law (Ruina, 1983) or composite laws (Kato & Tullis, 2001). Rate-weakening behavior is not explored either.

Our model results indicate that rate-strengthening faults are very sensitive to pore-pressure perturbations. SSEs arise after pore pressure perturbations with a broad range of characteristics (Figures 4 to 6 and Tables S1 to S3). Likewise, perturbations on faults over different rate-strengthening conditions ($1.1 < a/b < 2.5$) lead to SSEs (Figure S4). These results suggest that rate-strengthening friction properties may play a more important role in slow slip generation than commonly assumed, which implies a broader range of conditions favorable for SSE occurrence.

7 Open research

The numerical data used to produce the figures is available at `https://doi.org/10.5281/zenodo.7488074`.

Acknowledgments

This work was supported by the Rutherford Discovery Fellowship from the Royal Society of New Zealand and the Ministry of Business, Innovation and Employment (MBIE) grant to GNS (contract CO5X1605). Computing resources were provided by the New Zealand eScience Infrastructure (NeSI) high-performance computing facilities. The authors thank Dr. Eric Dunham and Alexis Saez for their suggestions in the modeling of the radial diffusion perturbation. Most figures use perceptually uniform color palettes from Crameri (2018).

Table 1. Model parameters used in this study.

Parameter	***Symbol***	***Value***
Characteristic slip distance	d_c	5 mm
Direct effect	a	0.005
Evolution effect	b	0.004
Background effective normal stress	σ	3 MPa (9 MPa)[a]
Shear modulus	μ	10 GPa (30 GPa)[a]
Characteristic size of process zone	$L_b = \mu d_c / b\sigma$	4.17 km
Reference friction coefficient	f_0	0.6
Reference slip velocity	V_0	10^{-6} m^2/s
Poisson's ratio	ν	0.25
Loading rate	V_{pl}	50 mm/yr[b]
Spatial resolution	Δx	0.39 km to 0.78 km

[a] σ and μ used in simulation cases shown in Figures 5 and 6b to 6d, except for modeled shallow Hikurangi SSEs. [b] Different V_{pl} were considered in Figure 6, see Table 4.

Table 2. Perturbation characteristics for representative models of shallow Gisborne SSEs under type I (Figure 2) and type II (Figure 3) perturbations. Perturbation period is 2 yrs for both cases.

	Perturbation parameters	**Symbol**	**Value in representative model**
Type I	Duration of pressurization phase	T	1.5 yrs
	Radius	R_0	33.75 km
	Max. Amplitude	$\Delta p_{\max}$	1.88 MPa
	Normalized length-scale	R_0/L_b	$\sim$8
	Normalized amplitude	$\Delta p_{\max}/a\sigma$	125
Type II	Fluid "injection" time	t_{inj}	30 days
	Hydraulic diffusivity (pressurization)	D	25 m^2/s
	Hydraulic diffusivity (depressurization)	D_b	40 m^2/s
	Cylinder radius	r_0	1 km
	Max. amplitude	$\Delta p_{\max}$	1.5 MPa
	Normalized length scale	$\sqrt{Dt_{\text{inj}}}/L_b$	1.93
	Normalized amplitude	$\Delta p_{\max}/a\sigma$	100

Table 3. Range of source properties of observed SSEs offshore Gisborne (taken from Ikari et al. 2020's catalog) compared with average properties of modeled SSEs from two representative models for type I and type II perturbation (Section 3). Obs. stands for observed. Note that to calculate SSE properties we set a velocity threshold (V_{thr}) of 2 mm/day, consistent with the resolution limit of GPS network for shallow Hikurangi SSEs (Section 4.1).

Source property	**Obs. SSEs offshore Gisborne**	**Model type I**	**Model type II**
Duration (days)	6-34	25.6 ± 0.03	26.7 ± 0.03
Magnitude (M_w)	6.2-6.5	6.2	6.1
Max. slip (cm)	4-27	10.0 ± 0.1	9.98 ±0.03
Recurrence interval (yrs)	∼2	2	2

Table 4. Plate rate (V_{pl}) and velocity threshold (V_{thr}) assumed for each target SSEs. V_{thr} represents the slip velocity threshold assumed to calculate SSE properties (Section 4.1). The highest V_{thr} (15 V_{pl}) is assumed for shallow Hikurangi SSEs, as they occur offshore, away from GPS networks. We set $V_{\text{thr}} = 3\ V_{\text{pl}}$ for all SSEs that occur beneath GPS networks. We take V_{pl} from (Hikurangi) Wallace et al. (2004), (Cascadia) McCaffrey et al. (2013), (Nankai) Miyazaki and Heki (2001) and (Guerrero) DeMets et al. (2010).

Target SSEs	V_{pl} **(mm/yr)**	$V_{\text{thr}}/V_{\text{pl}}$	V_{thr} **in mm/day**
Shallow Hikurangi	50 or 40[a]	15	2 or 1.6
Deep Hikurangi	40	3	0.33
Cascadia	40	3	0.33
Nankai	67	3	0.55
Guerrero	61	3	0.5

[a]We set $V_{\text{pl}} = 40$ mm/yr for southern Hikurangi margin (south of Hawkes Bay) and $V_{\text{pl}} = 50$ mm/yr for northern Hikurangi (offshore Gisborne), consistent with the change in convergence rates along the margin (Wallace et al., 2004).

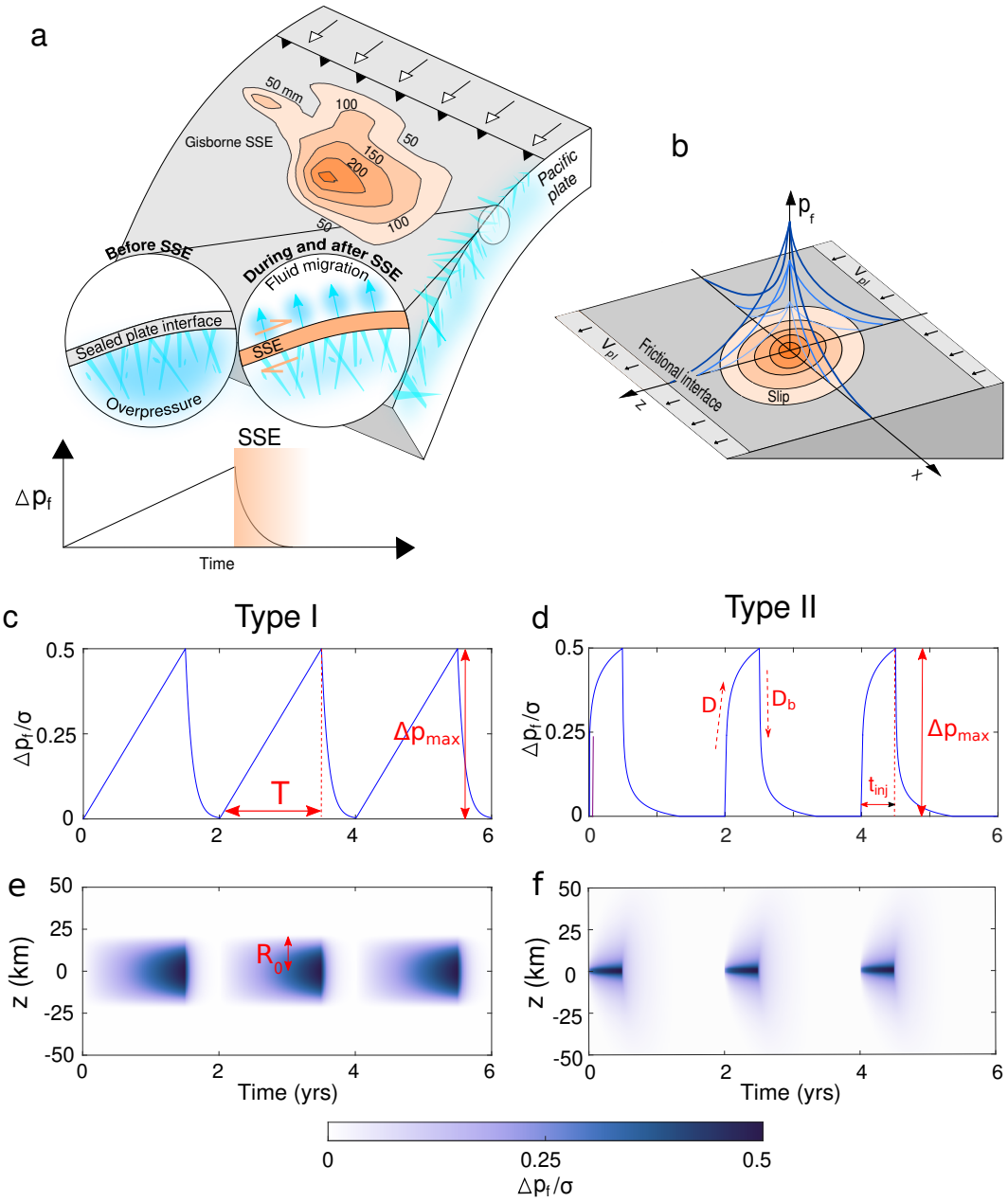

Figure 1. a) Schematic diagram representing a conceptual model of pore-pressure cycling during shallow Hikurangi SSEs, based on Warren-Smith et al. (2019). Orange contours show cumulative slip during 2016 shallow Gisborne SSE (Wallace et al., 2016). Thick blue lines indicate fractures. The bottom inset shows the inferred change in pore fluid pressure within the subducting Pacific slab during an SSE cycle (modified from figure 4a in Warren-Smith et al., 2019). (b) Schematic of our model setup showing pore-pressure increase at the fault center (blue lines; different shades indicate different time steps) and ensuing slip (orange contours) on the plate interface. (c - f) Examples of modeled pore fluid pressure changes for type I (c and e) and type II (d and f) perturbations. Temporal pore fluid pressure change is shown (c and d) at the fault center and (e and f) along z. Perturbation parameters shown are explained in Section 2.3.

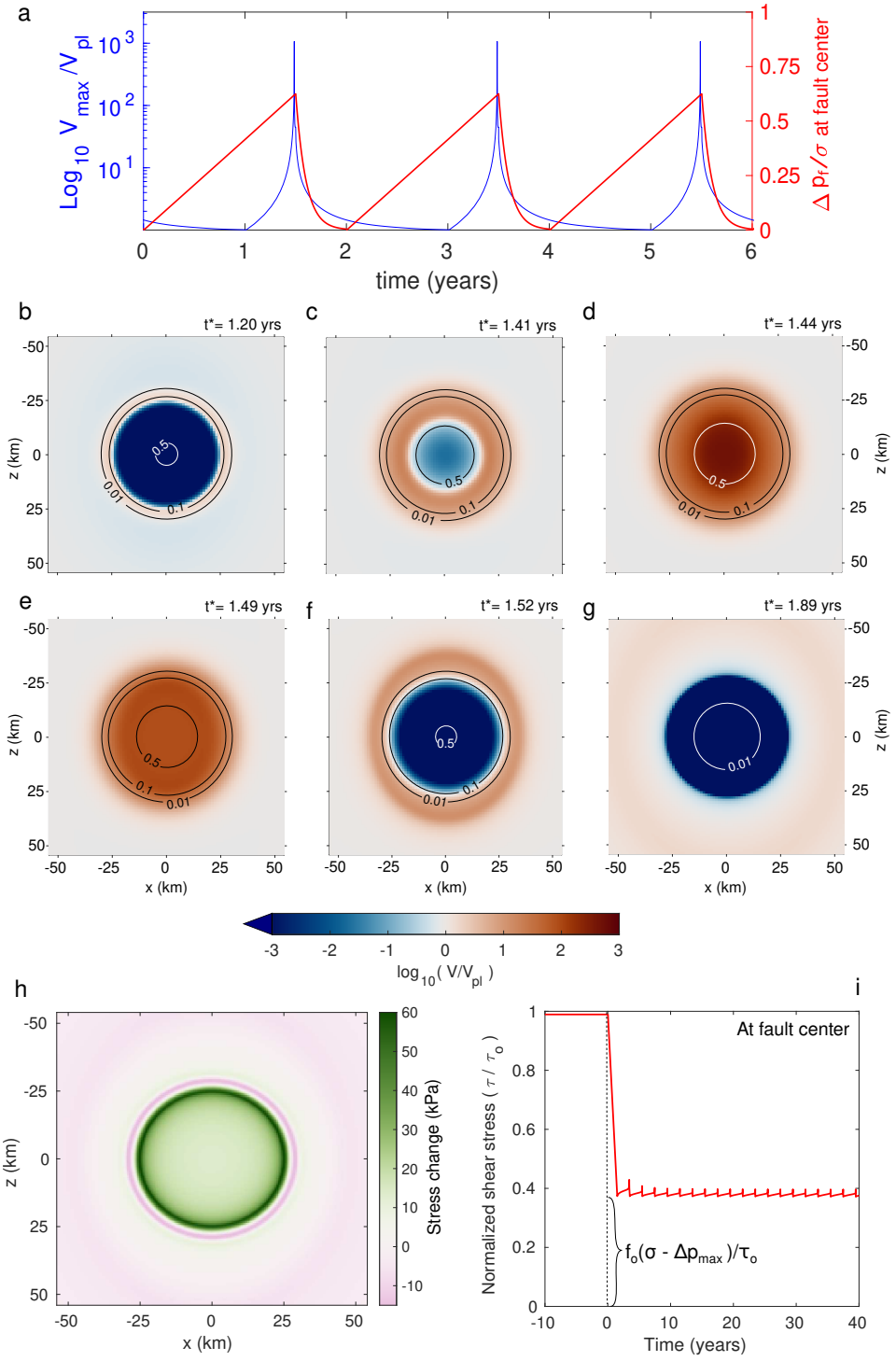

Figure 2. Representative model of shallow Gisborne SSEs for simulation under type I perturbation. (a) Temporal evolution of normalized maximum slip rate on the fault ($V_{\max}/V_{\rm pl}$, blue line) and normalized pore pressure change at the fault center ($\Delta p_{\rm f}/\sigma$, red line). (b-g) Snapshots of slip rate on the fault for an induced SSE during (b-e) pore-pressure increase and (f-g) pore pressure decrease. Solid lines indicate the contours of the normalized iso-pressure change, $\Delta p_{\rm f}/\sigma$. t^* shows the time since the start of the perturbation. (h) Shear stress change for a single induced SSE. The shear stress change is defined as the difference between the shear stress before and after the SSE. (i) Temporal evolution of normalized shear stress (τ/τ_o) at fault center, where τ_o is the initial shear stress. Dashed black line indicates the start of the perturbation. Shear stress decreases to the value of the fault strength at the start of the perturbation.

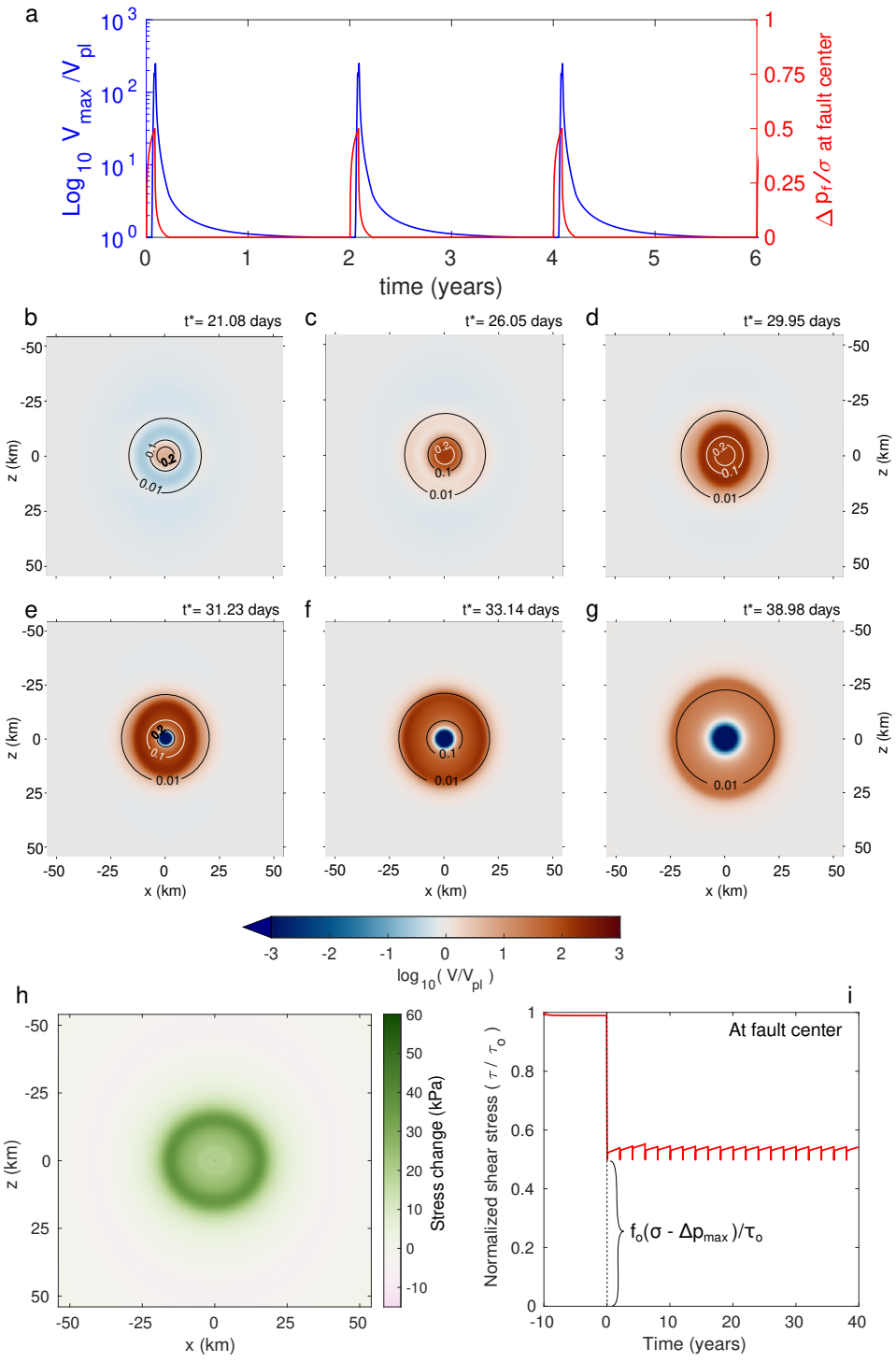

Figure 3. Representative model of shallow Gisborne SSEs for simulation under type II perturbation. (a) Temporal evolution of normalized maximum slip rate on the fault ($V_{\max}/V_{\rm pl}$, blue line) and normalized pore pressure change at the fault center ($\Delta p_{\rm f}/\sigma$, red line). (b-g) Snapshots of slip rate on the fault for an induced SSE during (b-d) pore-pressure increase and (e-g) pore-pressure decrease. Solid lines indicate the contours of the normalized iso-pressure change, $\Delta p_{\rm f}/\sigma$. t^* shows the time since the start of the perturbation. (h) Shear stress change for a single induced SSE. (i) Temporal evolution of normalized shear stress (τ/τ_o) at fault center. Shear stress decreases to the value of the fault strength at the start of perturbation, indicated by the dashed black line.

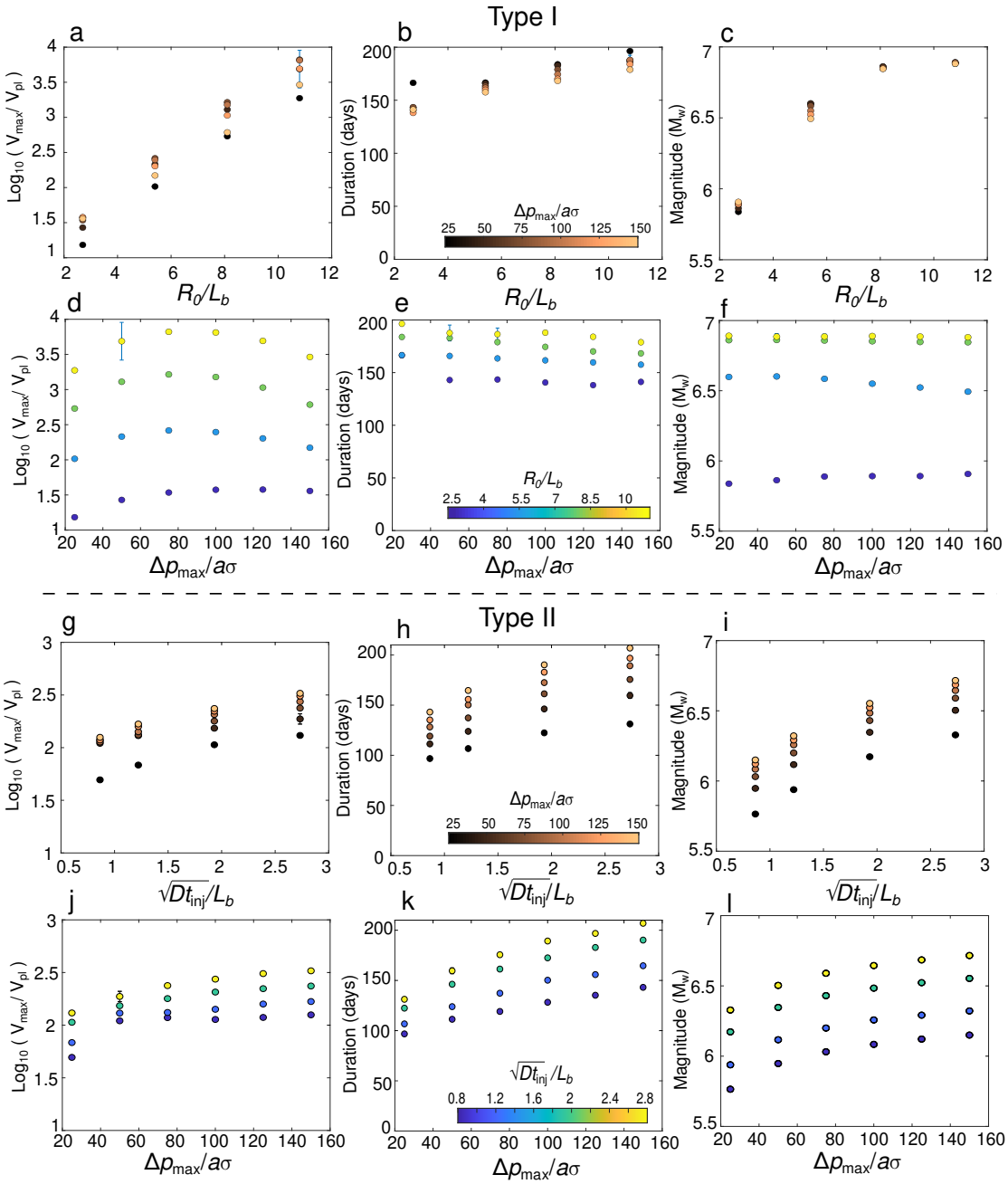

Figure 4. Average properties of SSEs induced by periodic perturbations in pore-pressure of (a-f) type I and (j-l) type II. Model parameters are given in Table 1. SSE properties are shown as a function of (a-c and g-i) the perturbation length scale (R_0/L_b or $\sqrt{Dt_{\rm inj}}/L_b$) for various values of the perturbation amplitude and as a function of (d-f and j-l) the perturbation amplitude ($\Delta p_{\rm max}/a\sigma$) for various values of the perturbation length scale. Vertical lines indicate standard deviation. For type II perturbation, we assume that $D_b/D = 1.1$ in all cases. A velocity threshold of $V_{\rm thr}$= 0.3 mm/day was assumed to calculate SSE properties (Section 4.1). Table S1 shows the range of parameters explored.

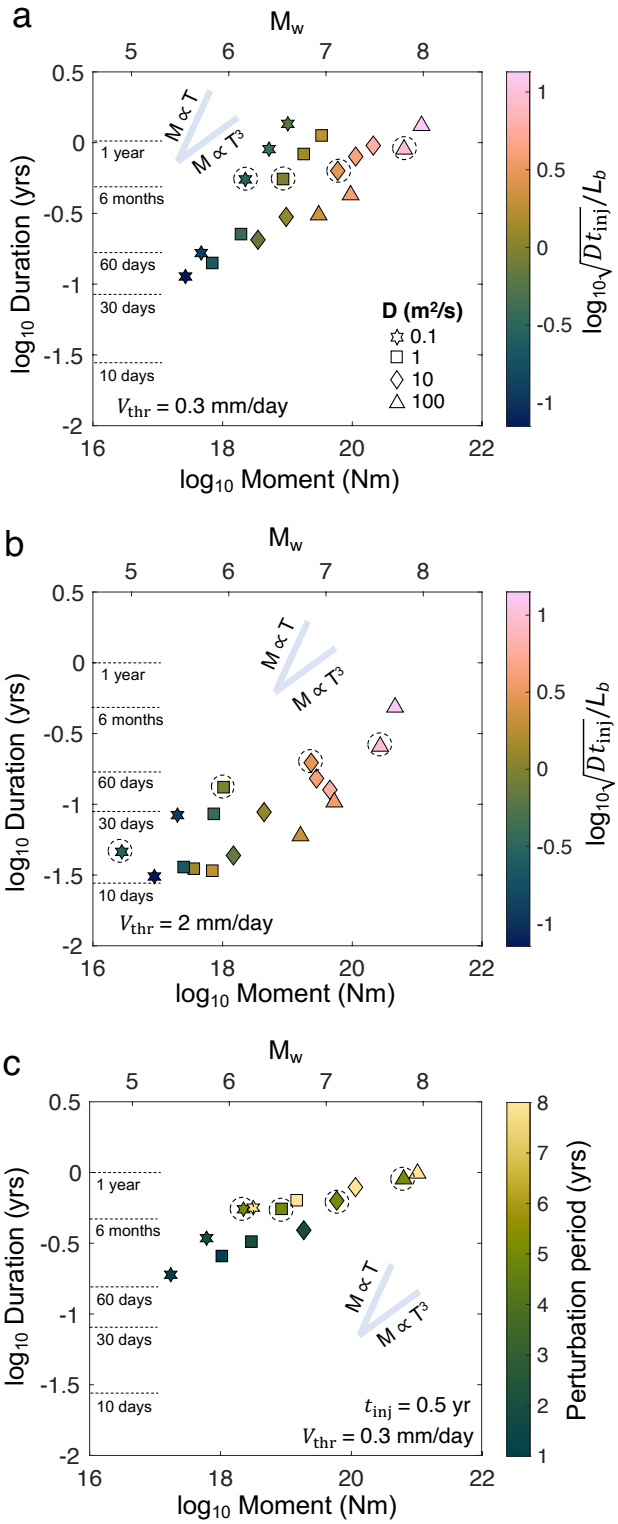

Figure 5. Source properties of induced SSEs for simulation cases under type II perturbation. SSE moment-duration for cases with (a) different perturbation size ($\sqrt{Dt_{\mathrm{inj}}}/L_b$), (b) higher V_{thr} = 2 mm/yr for same cases shown in (a) (V_{thr} = 0.3 mm/day for a and c), and (c) different perturbation period (assuming t_{inj}=0.5 yrs). t_{inj} ranges from 10 days to 2 yrs in (a) and (b). Dashed black circles indicate the same simulation cases. Markers shape correspond to different diffusivity values (D) as shown in (a). For reference, the linear and cubic moment-duration scaling trends (thick grey lines in a to c) are also included. Table S2 provides the perturbation characteristics of the simulations cases shown.

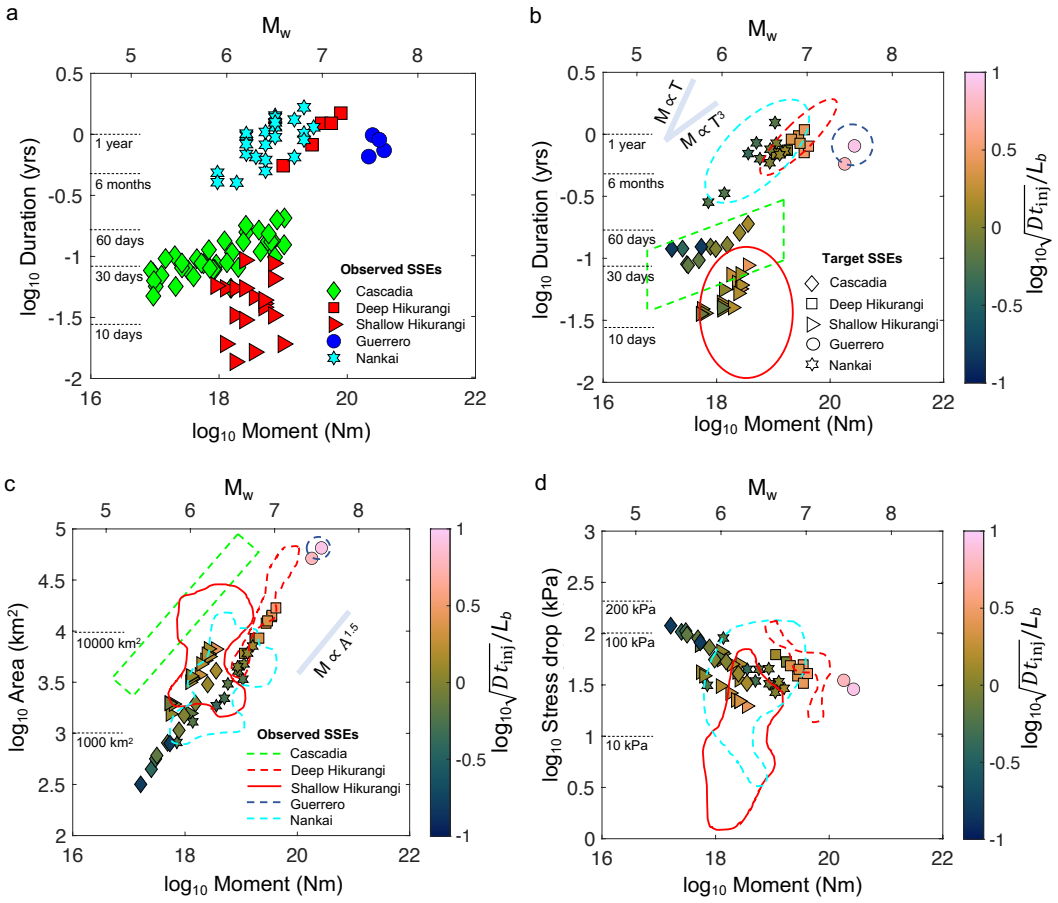

Figure 6. Comparison between observed and modeled source properties of SSEs from different subduction zones. (a) Observed moment and duration of shallow and deep Hikurangi SSEs (Ikari et al., 2020), Cascadia SSEs (Michel et al., 2019), Nankai SSEs (Takagi et al., 2019) and Guerrero SSEs (Radiguet et al., 2012, 2016). (b)-(c) Source properties of induced SSEs in simulation cases with different $\sqrt{Dt_{\mathrm{inj}}}/L_b$ (see also Figure S11 and Tables 4 and S3). Each shape corresponds to a different target SSE as shown in (b). The colored lines highlight the range of observed properties for a given target SSE, as shown in (c). For reference, the moment-duration and moment-area scaling trends (thick grey lines in b and c) are also included. Note that only stress drop for SSEs along Hikurangi (Ikari et al., 2020) and Nankai (Takagi et al., 2019) subduction zones were constrained by observations. For deep Hikurangi SSEs, we take the average stress drop between the different stages of the event shown in the catalog from Ikari et al. (2020). To compare observed Nankai SSE moments with our model results, we set $\mu = 30$ GPa, instead of 40 GPa, as reported by Takagi et al. (2019).

References

Ampuero, J.-P., & Rubin, A. M. (2008). Earthquake nucleation on rate and state faults–Aging and slip laws. *Journal of Geophysical Research: Solid Earth*, *113*, B01302. doi: 10.1029/2007JB005082.

Arnulf, A. F., Biemiller, J., Lavier, L., Wallace, L. M., Bassett, D., Henrys, S., ... Faverola, A. P. (2021). Physical conditions and frictional properties in the source region of a slow-slip event. *Nature Geoscience*, *14*, 334–340. doi: 10.1038/s41561-021-00741-0.

Audet, P., Bostock, M. G., Christensen, N. I., & Peacock, S. M. (2009). Seismic evidence for overpressured subducted oceanic crust and megathrust fault sealing. *Nature*, *457*(7225), 76–78. doi: 10.1038/nature07650.

Behr, W. M., & Bürgmann, R. (2021). What's down there? The structures, materials and environment of deep-seated slow slip and tremor. *Philosophical Transactions of the Royal Society A: Mathematical, Physical and Engineering Sciences*, *379*(2193), 20200218. doi: 10.1098/rsta.2020.0218

Bernaudin, M., & Gueydan, F. (2018). Episodic tremor and slip explained by fluid-enhanced microfracturing and sealing. *Geophysical Research Letters*, *45*(8), 3471-3480. doi: 10.1029/2018GL077586

Bhattacharya, P., Rubin, A. M., & Beeler, N. M. (2017). Does fault strengthening in laboratory rock friction experiments really depend primarily upon time and not slip? *Journal of Geophysical Research: Solid Earth*, *122*(8), 6389–6430. doi: 10.1002/2017JB013936.

Boulton, C., Niemeijer, A. R., Hollis, C. J., Townend, J., Raven, M. D., Kulhanek, D. K., & Shepherd, C. L. (2019). Temperature-dependent frictional properties of heterogeneous Hikurangi Subduction Zone input sediments, ODP Site 1124. *Tectonophysics*, *757*, 123–139. doi: 10.1016/j.tecto.2019.02.006.

Bürgmann, R. (2018). The geophysics, geology and mechanics of slow fault slip. *Earth and Planetary Science Letters*, *495*, 112-134. doi: 10.1016/j.epsl.2018.04.062

Cappa, F., Guglielmi, Y., Nussbaum, C., & Birkholzer, J. (2018). On the relationship between fault permeability increases, induced stress perturbation, and the growth of aseismic slip during fluid injection. *Geophysical Research Letters*, *45*, 11,012-11,020. doi: 10.1029/2018GL080233

Cappa, F., Scuderi, M. M., Collettini, C., Guglielmi, Y., & Avouac, J.-P. (2019). Stabilization of fault slip by fluid injection in the laboratory and in situ. *Science Advances*, *5*(3), eaau4065. doi: 10.1126/sciadv.aau4065

Carslaw, H., & Jaeger, J. (1959). *Conduction of heat in solids.* Clarendon Press, Oxford.

Cheng, A. H.-D. (2016). *Poroelasticity* (Vol. 27). Springer International Publishing. doi: 10.1007/978-3-319-25202-5

Condit, C. B., & French, M. E. (2022). Geologic evidence of lithostatic pore fluid pressures at the base of the subduction seismogenic zone. *Geophysical Research Letters*, *49*(12), e2022GL098862. doi: 10.1029/2022GL098862

Crameri, F. (2018). Geodynamic diagnostics, scientific visualisation and StagLab 3.0. *Geoscientific Model Development*, *11*(6), 2541–2562. doi: 10.5194/gmd-11-2541-2018.

Cruz-Atienza, V. M., Villafuerte, C., & Bhat, H. S. (2018). Rapid tremor migration and pore-pressure waves in subduction zones. *Nature Communications*, *9*, 2900. doi: 10.1038/s41467-018-05150-3

Dal Zilio, L., Lapusta, N., & Avouac, J.-P. (2020). Unraveling scaling properties of slow-slip events. *Geophysical Research Letters*, *47*(10), e2020GL087477. doi: 10.1029/2020GL087477.

DeMets, C., Gordon, R. G., & Argus, D. F. (2010). Geologically current plate motions. *Geophysical Journal International*, *181*(1), 1-80. doi: 10.1111/j.1365-246X.2009.04491.x.

Dieterich, J. H. (1979). Modeling of rock friction: 1. Experimental results and constitutive equations. *Journal of Geophysical Research: Solid Earth*, *84*(B5), 2161–2168. doi: 10.1029/JB084iB05p02161.

Dublanchet, P. (2019). Fluid driven shear cracks on a strengthening rate-and-state frictional fault. *Journal of the Mechanics and Physics of Solids*, *132*, 103672. doi: 10.1016/j.jmps.2019.07.015

Eijsink, A. M., & Ikari, M. J. (2022). Plate-rate frictional behavior of sediment inputs to the Hikurangi subduction margin: How does lithology control slow slip events? *Geochemistry, Geophysics, Geosystems*, *23*(6), e2022GC010369. doi: 10.1029/2022GC010369

Farge, G., Jaupart, C., & Shapiro, N. M. (2021). Episodicity and migration of low frequency earthquakes modeled with fast fluid pressure transients in the permeable subduction interface. *Journal of Geophysical Research: Solid Earth*, *126*, e2021JB021894. doi: 10.1029/2021JB021894

Frank, W. B., & Brodsky, E. E. (2019). Daily measurement of slow slip from low-frequency earthquakes is consistent with ordinary earthquake scaling. *Science advances*, *5*(10), eaaw9386. doi: 10.1126/sciadv.aaw9386.

Frank, W. B., Shapiro, N. M., Husker, A. L., Kostoglodov, V., Bhat, H. S., & Campillo, M. (2015). Along-fault pore-pressure evolution during a slow-slip event in Guerrero, Mexico. *Earth and Planetary Science Letters*, *413*, 135–143. doi: 10.1016/j.epsl.2014.12.051.

Gao, H., Schmidt, D. A., & Weldon, R. J. (2012). Scaling relationships of source parameters for slow slip events. *Bulletin of the Seismological Society of America*, *102*(1), 352–360. doi: 10.1785/0120110096.

Gosselin, J. M., Audet, P., Estève, C., McLellan, M., Mosher, S. G., & Schaeffer, A. J. (2020). Seismic evidence for megathrust fault-valve behavior during episodic tremor and slip. *Science Advances*, *6*, eaay5174. doi: 10.1126/sciadv.aay5174

Guglielmi, Y., Cappa, F., Avouac, J.-P., Henry, P., & Elsworth, D. (2015). Seismicity triggered by fluid injection-induced aseismic slip. *Science*, *348*(6240), 1224-1226. doi: 10.1126/science.aab0476

Heimisson, E. R., Dunham, E. M., & Almquist, M. (2019). Poroelastic effects destabilize mildly rate-strengthening friction to generate stable slow slip pulses. *Journal of the Mechanics and Physics of Solids*, *130*, 262-279. doi: 10.1016/j.jmps.2019.06.007

Hyndman, R. D., & Peacock, S. M. (2003). Serpentinization of the forearc mantle. *Earth and Planetary Science Letters*, *212*(3-4), 417–432. doi: 10.1016/S0012-821X(03)00263-2

Ide, S., Beroza, G. C., Shelly, D. R., & Uchide, T. (2007). A scaling law for slow earthquakes. *Nature*, *447*(7140), 76–79. doi: 10.1038/nature05780.

Ikari, M. J., Marone, C., Saffer, D. M., & Kopf, A. J. (2013). Slip weakening as a mechanism for slow earthquakes. *Nature geoscience*, *6*(6), 468–472. doi: 10.1038/ngeo1818

Ikari, M. J., Wallace, L. M., Rabinowitz, H. S., Savage, H. M., Hamling, I. J., & Kopf, A. J. (2020). Observations of laboratory and natural slow slip events: Hikurangi subduction zone, New Zealand. *Geochemistry, Geophysics, Geosystems*, *21*(2), e2019GC008717. doi: 10.1029/2019GC008717.

Kanamori, H., & Anderson, D. L. (1975). Theoretical basis of some empirical relations in seismology. *Bulletin of the seismological society of America*, *65*(5), 1073–1095.

Kato, N., & Tullis, T. E. (2001). A composite rate-and state-dependent law for rock friction. *Geophysical Research Letters*, *28*(6), 1103–1106. doi: 10.1029/2000GL012060.

Kita, S., Houston, H., Yabe, S., Tanaka, S., Asano, Y., Shibutani, T., & Suda, N. (2021). Effects of episodic slow slip on seismicity and stress near a

subduction-zone megathrust. *Nature Communications*, *12*, 7253. doi: 10.1038/s41467-021-27453-8

Lapusta, N., & Liu, Y. (2009). Three-dimensional boundary integral modeling of spontaneous earthquake sequences and aseismic slip. *Journal of Geophysical Research: Solid Earth*, *114*, B09303. doi: 10.1029/2008JB005934

Larochelle, S., Lapusta, N., Ampuero, J., & Cappa, F. (2021). Constraining fault friction and stability with fluid-injection field experiments. *Geophysical Research Letters*, *48*, e2020GL091188. doi: 10.1029/2020GL091188

Li, D., & Liu, Y. (2016). Spatiotemporal evolution of slow slip events in a nonplanar fault model for northern Cascadia subduction zone. *Journal of Geophysical Research: Solid Earth*, *121*(9), 6828–6845. doi: 10.1002/2016JB012857.

Liu, Y., & Rice, J. R. (2007). Spontaneous and triggered aseismic deformation transients in a subduction fault model. *Journal of Geophysical Research: Solid Earth*, *112*, B09404. doi: 10.1029/2007JB004930.f.

Liu, Y., & Rice, J. R. (2009). Slow slip predictions based on granite and gabbro friction data compared to GPS measurements in northern Cascadia. *Journal of Geophysical Research: Solid Earth*, *114*, B09407. doi: 10.1029/2008JB006142.

Mallick, R., Meltzner, A. J., Tsang, L. L. H., Lindsey, E. O., Feng, L., & Hill, E. M. (2021). Long-lived shallow slow-slip events on the Sunda megathrust. *Nature Geoscience*, *14*, 327-333. doi: 10.1038/s41561-021-00727-y

Marone, C. (1998). Laboratory-derived friction laws and their application to seismic faulting. *Annual Review of Earth and Planetary Sciences*, *26*(1), 643–696. doi: 10.1146/annurev.earth.26.1.643

Matsuzawa, T., Shibazaki, B., Obara, K., & Hirose, H. (2013). Comprehensive model of short-and long-term slow slip events in the Shikoku region of Japan, incorporating a realistic plate configuration. *Geophysical Research Letters*, *40*(19), 5125–5130. doi: 10.1002/grl.51006.

McCaffrey, R., King, R. W., Payne, S. J., & Lancaster, M. (2013). Active tectonics of northwestern U.S. inferred from GPS-derived surface velocities. *Journal of Geophysical Research: Solid Earth*, *118*(2), 709-723. doi: 10.1029/2012JB009473

Michel, S., Gualandi, A., & Avouac, J.-P. (2019). Similar scaling laws for earthquakes and Cascadia slow-slip events. *Nature*, *574*(7779), 522–526. doi: 10.1038/s41586-019-1673-6.

Miller, S. A. (2015). Modeling enhanced geothermal systems and the essential nature of large-scale changes in permeability at the onset of slip. *Geofluids*, *15*(1-2), 338-349. doi: 10.1111/gfl.12108

Miyazaki, S., & Heki, K. (2001). Crustal velocity field of southwest Japan: Subduction and arc-arc collision. *Journal of Geophysical Research: Solid Earth*, *106*(B3), 4305-4326. doi: 10.1029/2000JB900312

Muñoz-Montecinos, J., Angiboust, S., Garcia-Casco, A., Glodny, J., & Bebout, G. (2021). Episodic hydrofracturing and large-scale flushing along deep subduction interfaces: Implications for fluid transfer and carbon recycling (Zagros Orogen, southeastern Iran). *Chemical Geology*, *571*, 120173. doi: 10.1016/j.chemgeo.2021.120173

Nakajima, J., & Uchida, N. (2018). Repeated drainage from megathrusts during episodic slow slip. *Nature Geoscience*, *11*(5), 351–356. doi: 10.1038/s41561-018-0090-z.

Noda, H., Lapusta, N., & Kanamori, H. (2013). Comparison of average stress drop measures for ruptures with heterogeneous stress change and implications for earthquake physics. *Geophysical Journal International*, *193*(3), 1691-1712. doi: 10.1093/gji/ggt074

Peacock, S. M., Christensen, N. I., Bostock, M. G., & Audet, P. (2011). High pore pressures and porosity at 35 km depth in the Cascadia subduction zone. *Geology*, *39*(5), 471–474. doi: 10.1130/G31649.1

Perez-Silva, A., Kaneko, Y., Savage, M., Wallace, L., Li, D., & Williams, C. (2022). Segmentation of shallow slow slip events at the Hikurangi subduction zone explained by along-strike changes in fault geometry and plate convergence rates. *Journal of Geophysical Research: Solid Earth*, *127*(1), e2021JB022913. doi: 10.1029/2021JB022913

Perez-Silva, A., Li, D., Gabriel, A.-A., & Kaneko, Y. (2021). 3D Modeling of long-term slow slip events along the flat-slab segment in the Guerrero Seismic Gap, Mexico. *Geophysical Research Letters*, *48*(13), e2021GL092968. doi: 10.1029/2021GL092968.

Perfettini, H., & Ampuero, J.-P. (2008). Dynamics of a velocity strengthening fault region: Implications for slow earthquakes and postseismic slip. *Journal of Geophysical Research: Solid Earth*, *113*, B09411. doi: 10.1029/2007JB005398

Perfettini, H., Schmittbuhl, J., Rice, J. R., & Cocco, M. (2001). Frictional response induced by time-dependent fluctuations of the normal loading. *Journal of Geophysical Research: Solid Earth*, *106*(B7), 13455-13472. doi: 10.1029/2000JB900366

Radiguet, M., Cotton, F., Vergnolle, M., Campillo, M., Walpersdorf, A., Cotte, N., & Kostoglodov, V. (2012). Slow slip events and strain accumulation in the Guerrero gap, Mexico. *Journal of Geophysical Research: Solid Earth*, *117*, B04305. doi: 10.1029/2011JB008801.

Radiguet, M., Perfettini, H., Cotte, N., Gualandi, A., Valette, B., Kostoglodov, V., ... Campillo, M. (2016). Triggering of the 2014 M_w 7.3 Papanoa earthquake by a slow slip event in Guerrero, Mexico. *Nature Geoscience*, *9*(11), 829–833. doi: 10.1038/ngeo2817.

Rubin, A. M., & Ampuero, J.-P. (2005). Earthquake nucleation on (aging) rate and state faults. *Journal of Geophysical Research: Solid Earth*, *110*, B11312. doi: 10.1029/2005JB003686.

Ruina, A. (1983). Slip instability and state variable friction laws. *Journal of Geophysical Research: Solid Earth*, *88*(B12), 10359–10370. doi: 10.1029/JB088iB12p10359

Saffer, D. M., & Wallace, L. M. (2015). The frictional, hydrologic, metamorphic and thermal habitat of shallow slow earthquakes. *Nature Geoscience*, *8*, 594-600. doi: 10.1038/ngeo2490

Schwartz, S. Y., & Rokosky, J. M. (2007). Slow slip events and seismic tremor at circum-Pacific subduction zones. *Reviews of Geophysics*, *45*, RG3004. doi: 10.1029/2006RG000208.

Segall, P., Rubin, A. M., Bradley, A. M., & Rice, J. R. (2010). Dilatant strengthening as a mechanism for slow slip events. *Journal of Geophysical Research*, *115*, B12305. doi: 10.1029/2010JB007449

Shibazaki, B. (2003). On the physical mechanism of silent slip events along the deeper part of the seismogenic zone. *Geophysical Research Letters*, *30*, 1489. doi: 10.1029/2003GL017047

Shibazaki, B., Obara, K., Matsuzawa, T., & Hirose, H. (2012). Modeling of slow slip events along the deep subduction zone in the Kii Peninsula and Tokai regions, southwest Japan. *Journal of Geophysical Research: Solid Earth*, *117*(B6). doi: 10.1029/2011JB009083.

Shibazaki, B., Wallace, L. M., Kaneko, Y., Hamling, I., Ito, Y., & Matsuzawa, T. (2019). Three-dimensional modeling of spontaneous and triggered slow-slip events at the Hikurangi subduction zone, New Zealand. *Journal of Geophysical Research: Solid Earth*, *124*(12), 13250–13268. doi: 10.1029/2019JB018190.

Sibson, R. H. (1990). Conditions for fault-valve behaviour. *Geological Society, London, Special Publications*, *54*(1), 15–28. doi: 10.1144/GSL.SP.1990.054.01.02.

Sibson, R. H. (1992). Fault-valve behavior and the hydrostatic-lithostatic fluid pressure interface. *Earth-Science Reviews*, *32*(1-2), 141–144. doi: 10.1016/0012-8252(92)90019-P.

Sibson, R. H. (2013). Stress switching in subduction forearcs: Implications for overpressure containment and strength cycling on megathrusts. *Tectonophysics*, *600*, 142-152. doi: 10.1016/j.tecto.2013.02.035

Skarbek, R. M., & Rempel, A. W. (2016). Dehydration-induced porosity waves and episodic tremor and slip. *Geochemistry, Geophysics, Geosystems*, *17*, 442-469. doi: 10.1002/2015GC006155

Stehfest, H. (1970). Numerical inversion of Laplace transforms. *Communications of the ACM*, *13*(1), 47–49.

Sáez, A., Lecampion, B., Bhattacharya, P., & Viesca, R. C. (2022). Three-dimensional fluid-driven stable frictional ruptures. *Journal of the Mechanics and Physics of Solids*, *160*, 104754. doi: 10.1016/j.jmps.2021.104754

Takagi, R., Uchida, N., & Obara, K. (2019). Along-strike variation and migration of long-term slow slip events in the western Nankai subduction zone, Japan. *Journal of Geophysical Research: Solid Earth*, *124*(4), 3853–3880. doi: 10.1029/2019JB018037.

Tan, Y. J., & Marsan, D. (2020). Connecting a broad spectrum of transient slip on the San Andreas fault. *Science advances*, *6*(33), eabb2489. doi: 10.1126/sciadv.abb2489.

Tanaka, Y., Kato, A., Sugano, T., Fu, G., Zhang, X., Furuya, M., ... Ishihara, M. (2010). Gravity changes observed between 2004 and 2009 near the Tokai slow-slip area and prospects for detecting fluid flow during future slow-slip events. *Earth, Planets and Space*, *62*, 905-913. doi: 10.5047/eps.2010.11.003

van Keken, P. E., Hacker, B. R., Syracuse, E. M., & Abers, G. A. (2011). Subduction factory: 4. Depth-dependent flux of H_2O from subducting slabs worldwide. *Journal of Geophysical Research*, *116*, B01401. doi: 10.1029/2010JB007922

Wallace, L. M. (2020). Slow slip events in New Zealand. *Annual Review of Earth and Planetary Sciences*, *48*, 175–203. doi: 10.1146/annurev-earth-071719-055104.

Wallace, L. M., & Beavan, J. (2010). Diverse slow slip behavior at the Hikurangi subduction margin, New Zealand. *Journal of Geophysical Research: Solid Earth*, *115*, B12402. doi: 10.1029/2010JB007717.

Wallace, L. M., Beavan, J., McCaffrey, R., & Darby, D. (2004). Subduction zone coupling and tectonic block rotations in the North Island, New Zealand. *Journal of Geophysical Research: Solid Earth*, *109*, B12406. doi: 10.1029/2004JB003241.

Wallace, L. M., Webb, S. C., Ito, Y., Mochizuki, K., Hino, R., Henrys, S., ... Sheehan, A. F. (2016). Slow slip near the trench at the Hikurangi subduction zone, New Zealand. *Science*, *352*(6286), 701–704. doi: 10.1126/science.aaf2349.

Wang, W., Savage, M. K., Yates, A., Zal, H. J., Webb, S., Boulton, C., ... Wallace, L. (2022). Temporal velocity variations in the northern Hikurangi margin and the relation to slow slip. *Earth and Planetary Science Letters*, *584*, 117443. doi: 10.1016/j.epsl.2022.117443

Warren-Smith, E., Fry, B., Wallace, L., Chon, E., Henrys, S., Sheehan, A., ... Lebedev, S. (2019). Episodic stress and fluid pressure cycling in subducting oceanic crust during slow slip. *Nature Geoscience*, *12*(6), 475–481. doi: 10.1038/s41561-019-0367-x.

Wech, A. G., & Bartlow, N. M. (2014). Slip rate and tremor genesis in Cascadia. *Geophysical Research Letters*, *41*(2), 392-398. doi: 10.1002/2013GL058607

Xue, L., Li, H.-B., Brodsky, E. E., Xu, Z.-Q., Kano, Y., Wang, H., ... Huang, Y. (2013). Continuous permeability measurements record healing inside the wenchuan earthquake fault zone. *Science*, *340*(6140), 1555-1559. doi: 10.1126/science.1237237

Yang, Y., & Dunham, E. M. (2021). Effect of porosity and permeability evolution on injection-induced aseismic slip. *Journal of Geophysical Research: Solid Earth*,

126, e2020JB021258. doi: 10.1029/2020JB021258

Zal, H. J., Jacobs, K., Savage, M. K., Yarce, J., Mroczek, S., Graham, K., ... Henrys, S. (2020). Temporal and spatial variations in seismic anisotropy and V_p/V_s ratios in a region of slow slip. *Earth and Planetary Science Letters*, *532*, 115970. doi: 10.1016/j.epsl.2019.115970.

Zhu, W., Allison, K. L., Dunham, E. M., & Yang, Y. (2020). Fault valving and pore pressure evolution in simulations of earthquake sequences and aseismic slip. *Nature Communications*, *11*(1), 4833. doi: 10.1038/s41467-020-18598-z.